OPEN ACCESS

University of BRISTOL

Peer reviewed version

Link to published version (if available):
10.1016/j.jsv.2020.115276

Link to publication record in Explore Bristol Research
PDF-document

University of Bristol - Explore Bristol Research
General rights

Influence of boundary layer flow suction on trailing edge noise generation

Máté Szőke[a,b,*], Daniele Fiscaletti[a], Mahdi Azarpeyvand[a]

[a]*Faculty of Engineering, University of Bristol, Bristol, United Kingdom, BS8 1TR*
[b]*Aerospace and Ocean Engineering, Virginia Tech, Blacksburg, Virginia, USA, 24061*

Abstract

The effect of uniform inclined flow suction on an equilibrium turbulent boundary layer developing over a flat plate is experimentally investigated for aeroacoustic purposes. Simultaneous measurements of streamwise velocity with hot-wire anemometry, and surface pressure fluctuations using flush-mounted microphones were performed at various locations downstream of the flow control treatment. The paper discusses the effects of flow suction on the turbulent quantities describing the boundary layer, and the associated hydrodynamic pressure field to assess the effects of flow suction on trailing edge noise generation. Two parameters were varied, the inclination of the flow suction velocity (α) and the flow suction severity (σ). The former is the angle of flow suction with respect to the free-stream flow ($\alpha = 30°, 50°, 70°$ and $90°$), while the latter is the ratio of momentum deficit within the boundary layer to the momentum of flow suction ($\sigma = 2.5 - 9.1$). Flow suction reduces the height of the boundary layer, which results in an increase of mean shear. The flow energy content within the boundary layer is reduced by suction with the most significant amount of reduction is observed within the logarithmic region. A moderate energy increase is observed in the buffer layer. These effects strengthen with growing suction severity until $\sigma \approx 6$. Above this point, no further changes are observed in the turbulent quantities. The reduction in the size and energy content of the logarithmic layer is responsible for the reduction of the surface pressure fluctuations at mid-frequencies, while the increased energy content in the buffer layer increases the pressure spectral content at high frequencies. The estimates of the far-field trailing edge noise show that flow suction leads to a noise reduction at mid-frequencies with penalties observed at low and high frequencies. Flow suction at an angle of $\alpha = 70°$ and $\sigma \approx 6$ exhibits the best performance in reducing the estimated far-field overall noise levels. Above this point, further increasing the flow suction severity does not provide any additional noise reduction benefits.

Keywords: Trailing edge noise, flow control, aeroacoustics, noise reduction

*Corresponding author:
Email address:* `m.szoke@vt.edu` (Máté Szőke)

1. Introduction

The increasing demand for renewable energy has resulted in a dramatic growth of wind farms over the past few decades. However, stringent regulations on the noise pollution in several countries pose strict limitations to the allowed acoustic emissions of on-shore wind farm installations. This makes the reduction of wind turbine noise an urgent engineering task. Trailing edge (TE) noise in particular, which is aerodynamically generated when an aerofoil is in relative movement inside of a fluid [1–3], is the dominant noise component emitted by wind turbine blades [4, 5].

The physical understanding of TE noise and its modeling have been the object of several investigations, with the ultimate goal of developing techniques for its reduction. It was shown that as the hydrodynamic pressure field associated with the turbulent boundary layer passes over the TE, the pressure field scatters into sound in a dipole manner [1–3, 6, 7]. As a result of extensive research on TE noise during the 70s and the 80s, analytical [3, 6, 8, 9] and empirical [1] noise models became robust tools to predict the TE noise. Nonetheless, the development of flow control techniques for noise reduction only relying on analytical modelling is a rather challenging task. In addition, analytical models should be somehow validated [10]. Recently, computational fluid dynamics (CFD) and large-eddy simulations were used to predict the far-field noise in a number of studies [11–14]. However, due to the rather high Reynolds numbers, in the order of millions, associated with wind turbine blades, the numerical estimation of far-field TE noise is still computationally unfeasible. As a result, wind tunnel testing is often the only available resource to assess the noise emission levels of wind turbines, and to develop TE noise reduction strategies.

In general, two families of flow control techniques exist that can attenuate the far-field TE noise, namely, *passive* and *active techniques*. Changes introduced to the geometry of the TE can be classified as *passive* noise reduction techniques. Serrated trailing edges are one of the most widely studied passive TE noise reduction methods [10, 15–21], where the geometry of the straight trailing edge is most often replaced by triangulated wedges. These wedges were observed to scatter sound to the far-field at a reduced efficiency compared to straight trailing edges [20]. Further examples of passive techniques are TE brushes [22, 23], porous materials [24–30], surface treatments [31–35], shape optimization, and morphing [36]. Overall, the passive techniques are relatively simple and inexpensive, and their noise reduction performance can often be optimized for a given range of operating conditions (Reynolds number, angle of attack, etc.). *Active techniques*, on the other hand, introduce changes to the boundary layer flow to reduce the energy content of the hydrodynamic pressure field. Active techniques can offer higher aeroacoustic performance than passive techniques, and they can be tailored to changes of the working conditions. Their main drawback is that they require a supply

of external energy, which needs to be kept conveniently low to sustain efficient operation [37, 38]. While *passive techniques* received a high research interest over the past decades [10, 20, 29, 35], *active techniques* are still in their early stages of development [4, 5, 39–43]. It has been shown that *active techniques* can reduce the TE noise [5], but our understanding of their underlying noise reduction mechanism is still modest and superficial. Flow suction, which is utilized in this work as an active noise control technique, has been studied by Wolf *et al.* [5], Lutz *et al.* [39], Matera [40] and Arnold *et al.* [4, 41]. These works confirm that flow suction can reduce the TE noise of up to 5-10 dB, which over-performs the noise reduction capabilities of the passive techniques. Shedding light on the mechanism that drives the reduction of TE noise could lead to a significant improvement in the performance of flow control techniques.

Understanding the effects of flow suction on boundary layer turbulence is essential to utilize it efficiently as an active noise control technique. In their pioneering study, Antonia *et al.* [44] observed that flow suction increases the stability of the longitudinal coherence of the large-scale low-speed streaks within the turbulent boundary layer. Their dye flow visualizations revealed that flow suction reduces the average frequency of dye ejections from the wall into the outer region of the turbulent boundary layer. This effect is an indication of reduced turbulent activity within the boundary layer. Their work was followed by a series of experimental and numerical investigations on the effect of concentrated flow suction from a turbulent boundary layer at low Reynolds numbers, see Antonia *et al.* [45], Oyewola *et al.* [46–48], Park and Choi [49] and a more recent work of Kametani *et al.* [50]. These studies [45–48, 50] covered a wide range of suction rates (σ), which they defined as the ratio of momentum flux of flow suction and momentum flux of the boundary layer. A number of studies [46] reported that flow suction can re-laminarise the boundary layer at moderate momentum thickness Reynolds numbers ($Re_\theta < 660$). At higher Re_θ and severe suction rates ($\sigma > 5.5$), however, a clear indication of a laminar boundary layer was not observed [45–48], and the boundary layer at this state was described as pseudo-laminar.

The pioneering numerical work of Park and Choi [49] shed more light on the flow behavior downstream of the flow suction slit. Their direct numerical simulations showed that uniform flow suction can bring streamwise vortices closer to the wall, which then increases viscous diffusion. This effect resulted in the break-up of the turbulent structures and the reduction of turbulence intensities and Reynolds shear stresses downstream of the flow control section. They showed that downstream of the flow suction slit, the boundary layer thickness increases as an effect of momentum deficit within the boundary layer. Further downstream, they reported a drop in the boundary layer integral quantities. In general, the majority of the previous studies [44–50] focusing on boundary layer turbulence downstream of flow suction reported a flow suction

severity rate at which a saturation in the studied turbulence parameters was observed. Overall, the studies on flow suction reviewed here suggest that the flow suction area shall be placed upstream of the trailing edge in order to utilize its favorable effects on boundary layer turbulence.

In the present work, we assess the effects of *flow suction* on a turbulent boundary layer from an aeroacoustic point of view. Flow suction was applied upstream of the TE on a zero pressure gradient flat plate test rig. Signals were simultaneously acquired from a single sensor hot-wire probe and a number of flush mounted microphones, which were both positioned at the same streamwise location. These measurements were used to estimate the necessary physical quantities for the prediction of the far-field noise through Amiet's model [3], and therefore, the aeroacoustic performance of flow suction. As a secondary goal, we intend to clarify the relationship between the turbulence characteristics of the flow and the resulting surface pressure fluctuations at the TE, which are the main responsible quantities for far-field noise emission. This approach can reveal the underlying mechanism of how flow suction can reduce the TE noise.

2. Experimental Approach

Experiments were conducted on a zero pressure gradient flat plate test rig in the open-jet wind tunnel of the University of Bristol. The closed-loop wind tunnel has a circular nozzle with a diameter of 1.1 m, and a 2 m long test volume where it is capable of producing flow speeds up to 26 m/s with incoming flow turbulence intensity below 0.5 %. The flat plate test rig has a length of $L = 1$ m and a width of $W = 0.7$ m, and it ends in a sharp (12°) TE, see Fig. 1. An 80-grit sandpaper was mounted immediately after the plate semi-elliptical leading-edge to trigger the development of the turbulent boundary layer on the surface of the plate. Downstream of the flow tripping, the boundary layer passes over the suction area, where flow suction is applied in an open-loop manner of control. The rig is instrumented with flush-mounted microphones downstream of the flow suction area. Tests were carried out at the uniform flow velocity of $u_\infty = 15$ m/s, corresponding to a Reynolds number of $Re_L = 10^6$ based on the length of the plate ($Re_L = u_\infty L/\nu$).

2.1. Test Rig and Instrumentation

During the measurement campaigns, the surface pressure fluctuations and the streamwise component of the velocity were measured simultaneously in the vicinity of the TE (see Fig. 1) at locations BL1, BL2 and BL3 located 99, 58.5 and 4.5 mm upstream of the trailing edge, respectively. Flush-mounted Knowles FG-23329-P07 type microphones were used for the measurement of the surface pressure fluctuations. A total number of 21 pressure transducers were positioned along the streamwise and the spanwise directions,
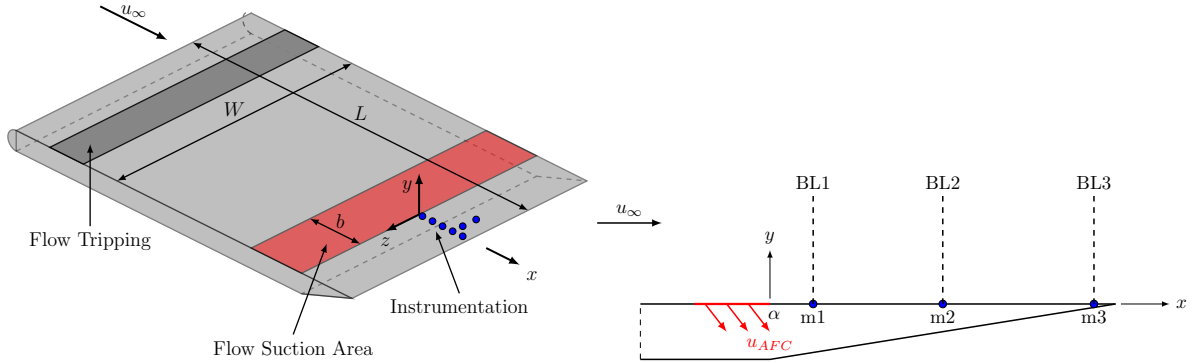
Figure 1: Schematics of the test rig and the simultaneous velocity and surface pressure measurements performed at locations BL1, BL2 and BL3, corresponding to $x/\delta_0 =, 0.6, 1.8$ and 4, respectively.

and in the vicinity of the TE, see Fig. 1. The streamwise component of the velocity was measured with hot-wire anemometry, to characterise the boundary layer flow downstream of the flow suction area. The Dantec 55P16 type single-sensor hot-wire probes were operated by a Dantec StreamWare Pro CTA91C10 module. The hot-wire probe was positioned above the flush-mounted microphones (see Fig. 1), and it was traversed along the wall-normal direction (y) using a ThorLabs LTS300/M stage which has a positioning accuracy of 5 μm. Data from the microphones and the hot-wire sensor were acquired using a National Instruments PXIe-4499 system at a sampling rate of $2^{16} = 65,536$ Samples/s for a time span of 16 seconds at each measurement location. Data processing was performed with the use of Python's SciPy package. For a more detailed description of the test rig, measurement apparatus, and the detailed quantification of the baseline case we refer to Refs. [42, 51, 52].

In the current work, the boundary layer properties are defined as follows. The boundary layer thickness, δ, is the distance between the wall $(y = 0)$ and the location where the mean velocity $(u(y))$ reaches 98 % of the free-stream velocity, i.e. $u(y = \delta) = 0.98u_\infty$. The boundary layer displacement thickness, δ^*, is obtained through the numerical integration of

$$\delta^* = \int_0^\delta \left(1 - \frac{u(y)}{u_\infty}\right) \mathrm{d}y. \tag{1}$$

The boundary layer momentum thickness, θ, is calculated in a similar manner as δ^* using

$$\theta = \int_0^\delta \frac{u(y)}{u_\infty} \left(1 - \frac{u(y)}{u_\infty}\right) \mathrm{d}y. \tag{2}$$

In addition, the subscript 0 refers to properties of the undisturbed boundary layer obtained at location BL1.

2.2. Flow Suction Parameters

Inclined flow suction is applied upstream of the sharp TE to perturb the boundary layer flow. In order to incline the flow suction, a honeycomb structure is installed within the surface of the plate, see Fig. 1. The size of the pores in the honeycomb structure are 5 mm × 5 mm, the thickness of the edges between the neighbouring cells is 0.5 mm, and the overall thickness of the honeycomb structure is 10 mm. Inclining the pores of the honeycomb structure ensures an inclined flow suction velocity (u_{AFC}) with respect to the free-stream flow (u_∞). Four different inclination angles (α) are considered in this work, namely, $\alpha = 30°, 50°, 70°$, and $90°$. The honeycomb pores were oriented towards the upstream direction thus creating a favorable condition for the boundary layer flow to enter the flow suction area, see Fig. 1. The suction area was covered by a wire mesh to ensure that the surface of the flow control section remains smooth. The wire mesh was made of square weaved stainless steel with a filament diameter of 0.1 mm and pore size of 0.2 mm. Preliminary measurements showed that the described configuration of the flow suction unit did not introduce any additional perturbation to the boundary layer.

The velocity of the flow suction (u_{AFC}) was measured using hot-wire anemometry with the sensor positioned at a distance of approximately 1 mm from the surface of the flow suction area. A radial fan, whose power was computer controlled, enabled us to smoothly adjust the flow suction velocity. From this, the flow suction velocity (u_{AFC}) was obtained and used to determine the flow control severity, σ. The flow control severity relates the momentum deficit of the boundary layer to the momentum of the flow control system. According to Antonia *et al.* [45], the *flow control severity* (σ) can be quantified as follows:

$$\sigma = \frac{u_{AFC}b}{u_\infty \theta_0} = C_Q \frac{b}{\theta_0}, \tag{3}$$

where u_{AFC} is the magnitude of the mean flow control velocity, $b = 30$ mm is the streamwise length of the flow control section, u_∞ is the velocity of the free-stream flow, $\theta_0 = 2.6$ mm is the momentum thickness of the non-disturbed boundary layer and $C_Q = u_{AFC}/u_\infty$ is the mass flow coefficient.

Figure 1 gives the geometrical description of the rig and provides the definition of the coordinate system. The coordinate system consists of the streamwise (x), the wall-normal (y), and the spanwise (z) directions, and its origin is at the mid-span of the plate, at the downstream edge of the active flow control section.

Two different sets of measurements were performed. In the first set of measurements, signals from all flush-mounted microphones were simultaneously recorded for a wide range of flow suction velocities ($u_{AFC} = 0.2 - 0.9u_\infty$) and flow control angles ($\alpha = 30°, 50°, 70°$ and $90°$). During the second set of

measurements, the streamwise velocity was measured with hot-wire anemometry along the whole wall-normal span of the turbulent boundary layer thickness, at three different streamwise locations, marked as BL1, BL2 and BL3, see the dashed lines in Fig. 1. At BL1, BL2 and BL3, the streamwise velocity and surface pressure fluctuations were recorded simultaneously to develop a comparative analysis of the turbulence characteristics and of the surface pressure fluctuations. Measurements of surface pressure fluctuations were made with the microphones marked by m1, m2 and m3 in Fig. 1.

2.3. Amiet's Trailing Edge Noise Model

The direct measurement of the far-field TE noise requires the use of an anechoic wind tunnel. Nonetheless, several physical models were developed in the last few decades [1, 3, 8], which estimate the far-field noise from the flow characteristics. According to these models, pressure and velocity measurements from conventional wind tunnels can be used as input parameters for the aforementioned models to confidently estimate the far-field TE noise. In the current work, Amiet's model [3] was used.

Amiet's model states that the noise (S_{pp}) at the far-field distance from the TE center-line of the flat plate ($x, y, z = 0$), can be estimated with the following equation:

$$S_{pp}(x, y, z = 0, f) = \left(\frac{fLy}{4\pi c_0 \xi^2} \right)^2 \frac{W}{2} |\mathcal{L}|^2 \Lambda_z(f)\phi_{pp}(f), \tag{4}$$

where f denotes frequency, c_0 is the speed of sound, $\xi^2 = x^2 + (1 - u_\infty/c_0)^2 y^2$ is the convection-corrected far-field observer position, L is the length of the plate (chord), W is the width of the plate, $\mathcal{L}$ is the gust response transfer function [53], Λ_z and ϕ_{pp} are, respectively, the spanwise extent of the turbulent structures within the boundary layer, and the power spectrum of the surface pressure fluctuations near the TE. Amiet's model works under the assumption of stationary turbulence. A more detailed description and the derivation of the model is given by Amiet [3, 6]. According to Amiet's model, the product $\Lambda_z \phi_{pp}$ drives the far-field noise emission. Therefore, the reduction of this product is the ultimate goal of every noise attenuation technique.

The surface pressure power spectrum (ϕ_{pp}) was directly measured in the current work, while the spanwise extent of the turbulent structures (Λ_z) could be calculated from surface pressure fluctuations as follows [3]:

$$\Lambda_z(f) = \int_0^\infty \sqrt{\gamma_z^2(f, \zeta)} \mathrm{d}\zeta, \tag{5}$$

where $\gamma_z^2(f, \zeta)$ represents the spanwise cross-spectrum of surface pressure fluctuations acquired from two

microphones located in the proximity to the TE, with a spanwise separation distance of $\zeta = \Delta z$. The cross-spectrum (coherence) could be interpreted as the spanwise extent of turbulent structures. In the current work, the spanwise coherence was measured at a streamwise distance of $0.4\delta_0$ upstream the TE, see Fig. 1. At this streamwise location, the thickness of the trailing edge is sufficiently large to fully embed the microphones into the rig, therefore they do not introduce any disturbances to the flow traveling below the plate. To calculate the spanwise coherence at different Δz, microphone signals acquired at three spanwise spacings were considered, namely at $\Delta z/\delta_0 = 0.12, 0.26$ and 0.38, from the array of spanwise pressure transducers located at $x/\delta_0 = 3.6$, near the TE. From this, the estimation of Λ_z was possible from Eq. (5) using a trapezoidal integration scheme.

3. Results

In this section, the aeroacoustic performance of flow suction is firstly investigated by estimating the far-field noise as predicted using Amiet's TE noise model [3]. Secondly, we focus on the changes that flow suction produces to the turbulence statistics within the boundary layer (BL). Moreover, we intend to quantify how the variations of the turbulence statistics from flow suction impact the hydrodynamic pressure field. The effects of these variations on the observed far-field TE noise generation are the ultimate object of the present investigation.

3.1. Estimates of Far-field Noise

According to Amiet's model [3], the product between the surface pressure spectra (ϕ_{pp}) and the spanwise extent of the turbulent length scales (Λ_z) drives the generation of far-field TE noise. The surface pressure spectra was measured in the close vicinity of the TE using microphone m3, see Fig. 1. The spanwise extent of the turbulent length scales was obtained as described in Section 2.3. From this, we obtained the predicted far-field TE noise using Amiet's model [3].

Figure 2 presents the far-field noise (S_{pp}) estimated using Amiet's model 1 m above the TE, for all considered cases of α and σ. For all cases, the harmonics observed above 400 Hz are a result of Amiet's trailing edge noise model. In particular, the gust response transfer function ($|\mathcal{L}|^2$) provides the shape of the far-field noise results.

Overall, flow suction shows a significant reduction of the far-field noise (S_{pp}) at mid-frequencies and a mild increase at low and high-frequencies. For $\alpha = 30°$, the frequency band where a reduction is observed ranges between 200 Hz and 1-2 kHz. The extent of the frequency band where noise attenuation is obtained
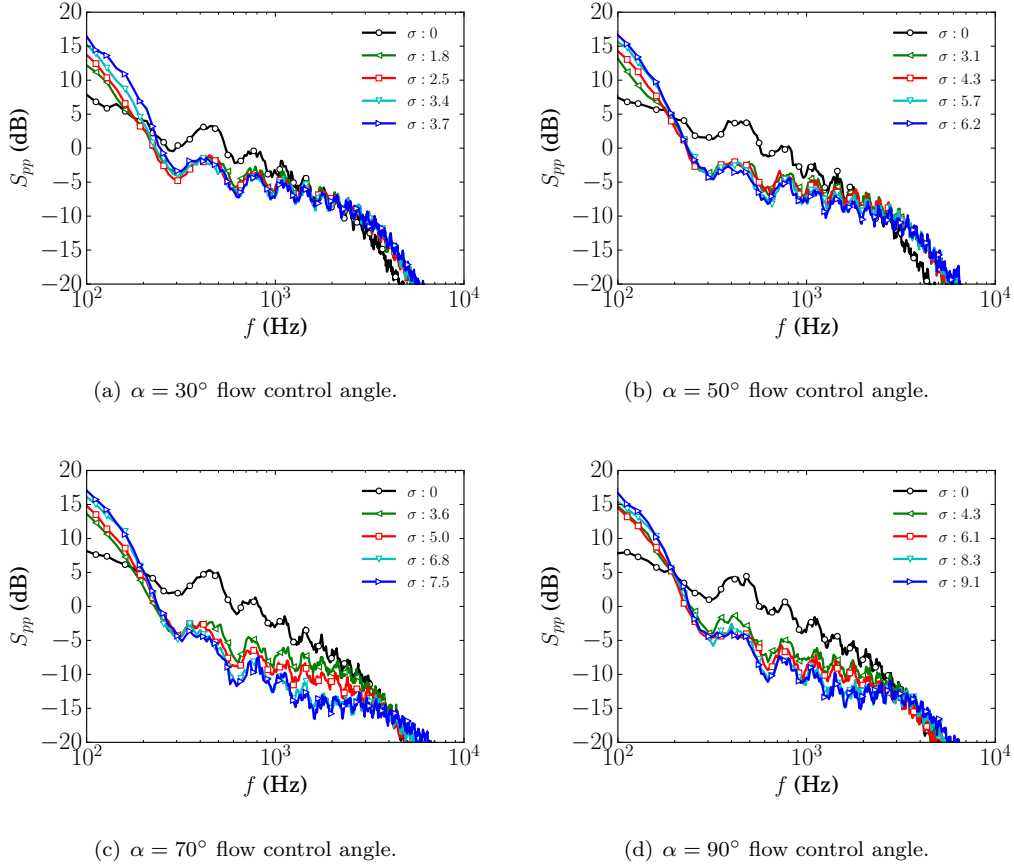
(a) $\alpha = 30°$ flow control angle.

(b) $\alpha = 50°$ flow control angle.

(c) $\alpha = 70°$ flow control angle.

(d) $\alpha = 90°$ flow control angle.

Figure 2: Estimation of far-field noise at flow control angles (a) $\alpha = 30°$, (b) $\alpha = 50°$, (c) $\alpha = 70°$ and (d) $\alpha = 90°$ using Amiet's noise model with the observer located at a vertical distance of 1 m above the TE.

enlarges with increasing flow suction severity, σ. On the other hand, the range of low frequencies where flow suction fails remains invariably confined to frequencies lower than 200 Hz, independent of the flow control severity (σ) and of the angle (α). Therefore, the frequency range where a reduction of the estimated far-field noise is achieved increases with increasing σ. The increase in the predicted far-field noise at low frequencies will be further investigated in Section 3.3. When comparing Fig. 2(c) and 2(d), i.e. flow suction at $\alpha = 70°$ and $\alpha = 90°$, it can be seen that flow suction at $\alpha = 70°$ is more efficient in reducing the far-field noise than at $\alpha = 90°$.

Additionally, the far-field noise was also calculated for an observer located at 1 m radius from the TE with varying polar angles of $\theta = 0° - 180°$. The estimated overall sound pressure level (OASPL, dB) was calculated by integrating S_{pp} over the frequency range of $100 - 10,000$ Hz, which is the frequency range of operation for the flush-mounted microphones used in this study. Results are shown in Fig. 3, at different polar angles, Θ. In general, an abatement of OASPL is observed when flow suction is applied ($\sigma > 0$). This

9

(a) $\alpha = 30°$ flow control angle.

(b) $\alpha = 50°$ flow control angle.

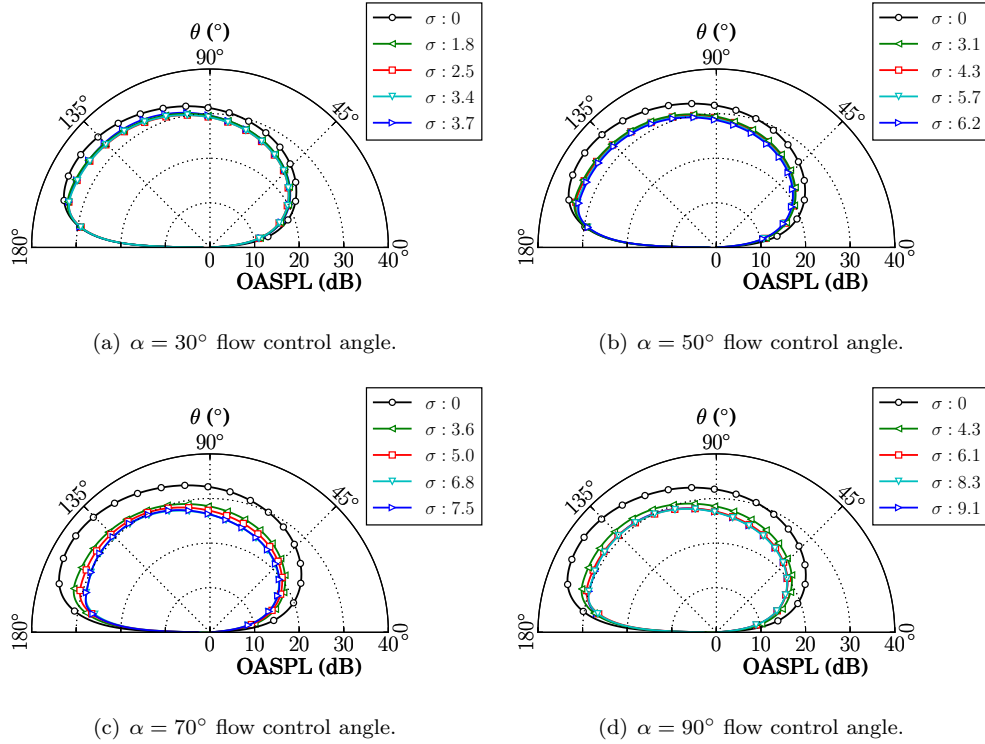(c) $\alpha = 70°$ flow control angle.

(d) $\alpha = 90°$ flow control angle.

Figure 3: Estimation of far-field noise overall sound pressure level at flow control angles (a) $\alpha = 30°$, (b) $\alpha = 50°$, (c) $\alpha = 70°$ and (d) $\alpha = 90°$ using Amiet's TE noise model with the observer located at different polar angles with a radial distance of 1 m above the TE.

indicates that the broadband noise reduction at mid-frequencies is dominant, see Fig. 2. In agreement with S_{pp}, as the flow suction severity (σ) and flow control angle (α) grow, the OASPL undergoes a decrease. Flow suction at $\alpha = 70°$ offers the best performance in reducing the OASPL levels, where up to 5 dB of noise reduction is estimated when $\sigma > 6$. Above this threshold ($\sigma \approx 6$), further increasing σ does not provide any further reduction of the estimated far-field noise. Therefore, based on these estimates of S_{pp} and OASPL, applying uniform flow suction at a flow control angle $\alpha = 70°$ with a flow control severity $\sigma \approx 6$ appears to offer the best aeroacoustic performance.

3.2. The Effects of Flow Suction on the Turbulent Statistics of the Boundary Layer

From the estimates of the far-field noise, it is found that $\alpha = 70°$ and $\sigma \approx 6$ offers the best aeroacoustic performance in far-field noise reduction. In the following, we seek an explanation for how flow suction reduces noise, and why the best aeroacoustic performance is obtained at the aforementioned configuration. To understand the effects of uniform flow suction on the turbulent boundary layer, the developing flow pattern is firstly investigated by means of turbulent statistics obtained at locations BL1, BL2 and BL3, see

10

Fig. 1. Because the turbulence statistics were found to have a similar behavior for all cases of α and σ, the results of $\alpha = 30°$ and $70°$ only are discussed in the followings.

α [°]	σ [-]	C_Q [-]	δ [mm]			δ^* [mm]			θ [mm]			u_τ [m/s]		
			BL1	BL2	BL3	BL1	BL2	BL3	BL1	BL2	BL3	BL1	BL2	BL3
-	0	0	29.5	30.2	30.5	3.81	3.61	3.69	2.57	2.59	2.63	0.617	0.618	0.622
30	2.5	0.28	57.0	46.0	12.5	3.69	2.70	1.20	3.08	2.21	2.01	0.692	0.679	0.685
30	3.7	0.42	58.1	49.4	10.1	3.84	2.42	1.30	3.23	1.98	1.12	0.596	0.623	0.632
70	5.0	0.57	60.4	54.7	3.0	3.76	2.58	0.25	3.35	2.14	0.17	0.622	0.656	0.751
70	7.5	0.85	63.4	61.1	1.2	4.69	3.21	0.31	4.12	2.65	0.16	0.642	0.604	0.740

Table 1: Boundary layer properties obtained at the angles of flow suction $\alpha = 30°$ and $70°$, at locations BL1, BL2 and BL3, corresponding to $x/\delta_0 = 0.6, 1.8$ and 4, respectively.

The flow behavior in the vicinity of the trailing edge was studied prior to investigating the effects of flow suction on boundary layer turbulence. Our thorough flow assessment analysis, consisting of hot-wire anemometry, static pressure (not presented here for brevity), and unsteady surface pressure measurements, found pieces of evidence that a zero pressure gradient turbulent boundary layer develops over the surface of the flat plate test rig. These observations confirmed that the flat plate test rig is a suitable tool to study the aeroacoustic effects of flow suction. For a more detailed analysis of the baseline case, we refer to Ref. [52].

To investigate the turbulence properties of the boundary layer, the streamwise velocity was measured at BL1, BL2 and BL3 along the wall-normal direction, corresponding to $x/\delta_0 = 0.6.1.8$ and 4, respectively. Boundary layer parameters, such as boundary layer thickness (δ), displacement thickness (δ^*), momentum thickness (θ) and friction velocity (u_τ) are given in Table 1 for varying α and σ cases. To study the effects of flow suction on the different regions of the boundary layer, namely, buffer, logarithmic and wake regions, the dimensionless velocity profiles (u^+) are presented in Fig. 4 as a function of the dimensionless wall distance (y^+). The + superscript denotes normalization by inner boundary layer quantities, i.e. $u^+ = \bar{u}/u_\tau$ and $y^+ = yu_\tau/\nu$. The dimensionless velocity (u^+) and dimensionless wall distance (y^+) are found iteratively by changing the friction velocity (u_τ) until a minimum discrepancy is reached between the measured and Spalding's empirical [54] velocity profile for the baseline case ($\sigma = 0$) and the viscous sublayer ($u^+ = y^+$) for $\sigma > 0$. This optimization was performed over a limited range of y^+, namely, for $\sigma = 0$ the discrepancy is minimized between $y^+ = 10$ and 300, while it is limited to $y^+ < 30$ for $\sigma > 0$. The boundary layer structures are identified with the help of Spalding's equation [54] for $\sigma = 0$, see black dashed lines in Fig. 4. A portion of the buffer layer is resolved below $y^+ < 20$. The logarithmic layer is located between $20 < y^+ < 300$, followed by the wake layer $300 < y^+ < 2000$, until the mean velocity reaches the value of the free-stream

velocity. The observed extent of these regions within the boundary layer match well with the numerical data provided by Schlatter and Örlü [55], at a similar Reynolds number ($Re_\theta = 3800$).
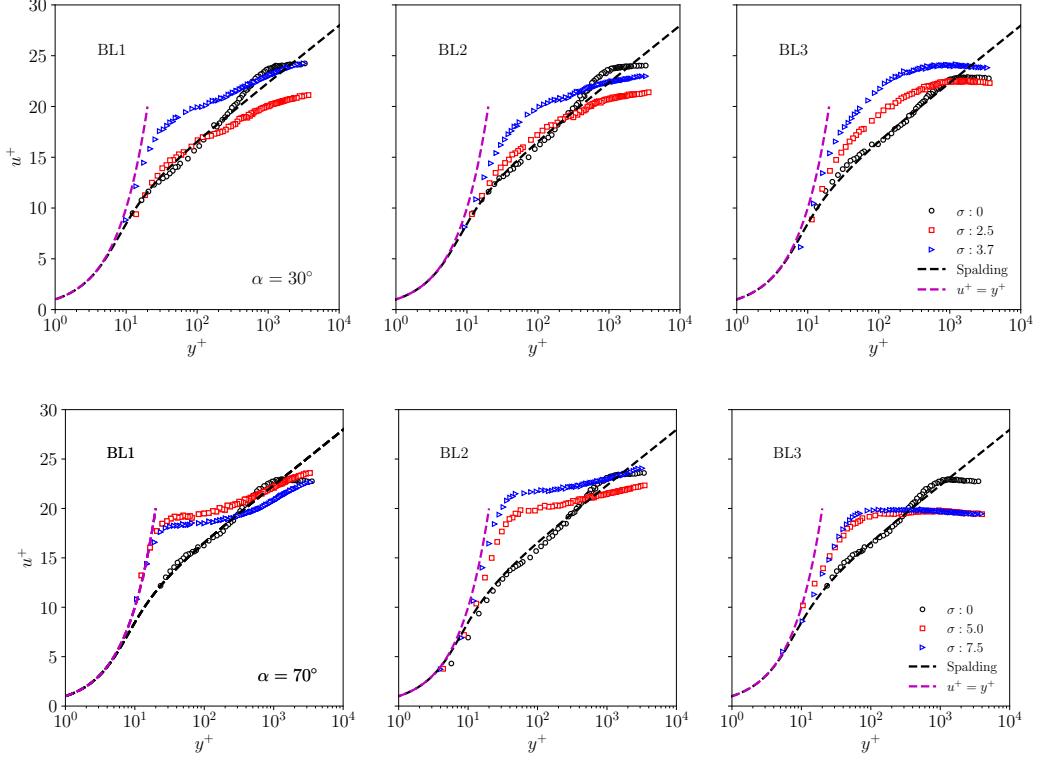

Figure 4: Dimensionless velocity profiles at flow control angles $\alpha = 30°$ and $\alpha = 70°$, obtained at locations BL1, BL2 and BL3.

The dimensionless velocity results in Fig. 4 reveal that flow suction significantly affects the structure of the boundary layer downstream of the flow control section (BL1-BL3). Therefore, the structure of the boundary layer is expected to change significantly. At BL1 ($x/\delta_0 = 0.6$), at the lowest angle of flow suction ($\alpha = 30°$) and at the lowest suction severity ($\sigma = 2.5$), the buffer layer follows the properties of the baseline case, which is in agreement with previous studies [45]. However, a quick recovery of the buffer layer was reported immediately downstream of the flow control section in Refs. [45, 46, 49]. The lowest amount of flow suction ($\sigma = 2.5$) efficiently reduces the span of the logarithmic layer at BL1 to the approximate range of $20 < y^+ < 100$, see Fig. 4. Similar observations can be made in the case of $\alpha = 30°$ for both $\sigma = 2.5$ and 3.7 rates at location BL2 ($x/\delta_0 = 1.8$). At BL3, on the other hand, the dimensionless velocity (u^+) deviates more from the baseline case compared to BL1 and BL2. A possible explanation for this can be that the TE affects the turbulence properties of the boundary layer at BL3.

Analogous observations can be made for $\alpha = 70°$ and at higher rates of flow severity, see Fig.4. At

12

BL1 and at low dimensionless wall distances ($y^+ < 20$), the u^+ profiles follow the shape of the viscous layer ($u^+ = y^+$). Above this region, the results suggest the presence of an inhomogeneous logarithmic layer, because the wake layer is not observed immediately. The larger extent of the viscous layer suggests a tendency towards laminar boundary layer behavior at all streamwise locations under analysis. Oyewola *et al.* [46] studied a turbulent boundary layer characterized with a lower Reynolds number ($Re_\theta \approx 600$) and observed a pseudo-laminar boundary layer at severe ($\sigma \approx 5.5$) suction rates. In our case, a similar behavior to that of Oyewola *et al.* [46] is observed, but a clear evidence of the presence of a laminar boundary layer, such as Tollmien–Schlichting waves, was not found. Only a *saturation* in the boundary layer shape at $\sigma \approx 6$ is observed, to which similar observations have been reported in previous flow suction studies [44–50].

At locations BL2 and BL3, the results reveal that the wall-normal extent of the logarithmic layer is significantly reduced, therefore, it can be expected that the turbulence properties in the logarithmic layer are also affected by flow suction. The results suggest that a saturation in the behavior of the boundary layer profiles can be reached at $\sigma \approx 6$. Above $\sigma \approx 6$, the effects of flow control are preserved at farther downstream locations with respect to BL1. This can be understood from the $u^+(y^+)$ profiles significantly departing from Spalding's equation at BL2 and BL3. Table 1 also reveals that the boundary layer thickness (δ) significantly reduces at BL3. From a general point of view, within a thinner boundary layer, the flow reaches the free-stream velocity over a shorter wall-normal span, which results in a larger mean shear ($d\bar{u}/dy$). The currently observed behavior of the dimensionless velocity profiles agrees well with the previous observations presented at similar streamwise locations (x/δ_0) by Antonia *et al.* [45] and Oyewola *et al.* [46].

The root mean square (rms) of the velocity enables us to study the effects of flow suction on the flow energy content within the turbulent boundary layer. Figure 5 presents the root mean square velocity profiles as a function of dimensionless wall distance (y^+), at $\alpha = 30°$ and $70°$, at BL1, BL2 and BL3. Analogous to the dimensionless velocity profiles shown in Fig. 4, the u_{rms} results also reveal that uniform flow suction significantly affects the energy content throughout the entire span of the turbulent boundary layer, therefore not only the near-wall region. Downstream of the flow control treatment, i.e. at BL1-BL3, the energy content within the boundary layer is significantly lower over the entire extent of the boundary layer for all cases of α and σ as a consequence of flow suction. Therefore, flow suction is effective in reducing the turbulent kinetic energy in the boundary layer over the entire range of wall-normal locations. The u_{rms} profiles as a function of y^+ reveal which regions of the flow lose or gain energy as a consequence of flow suction. According to Amiet's model, the far-field noise is proportional to the energy content of the surface pressure fluctuations. In general, it can be expected that a reduction in the flow energy content (u_{rms}) leads

13

to a reduction in the surface pressure energy content [56]. The analysis of the u_{rms} profiles and, therefore, the turbulent kinetic energy within the flow could clarify the physical mechanism by which flow suction reduces the far-field noise.

In general, the energy distribution of the baseline boundary layer ($\sigma = 0$) indicates that two peaks exist in the u_{rms} profile. An inner peak can be observed in the buffer layer in the vicinity of $y^+ \approx 20 - 30$, and an outer peak, that is visible at the upper edge of the logarithmic layer, at $y^+ \approx 200 - 300$. The inner peak is associated with the small-scale near-wall energetic turbulent motions, whereas the outer peak is related to the large-scale structures of the outer region (see Pope [56] and Smits *et al.* [57]).

Figure 5 shows that flow suction significantly attenuates u_{rms}. Surprisingly, flow suction is more effective in reducing the energy content of the outer peak than the inner peak. The larger is the suction severity, the larger is the attenuation of the outer peak. The outer peak is observed to disappear above $\sigma \approx 6$ at BL1, which is in agreement with previous observations of Oyewola *et al.* [46], who reported pseudo-laminarisation above $\sigma = 5.5$ for a turbulent boundary layer associated with a low Reynolds number ($Re_\theta \approx 600$). As the dimensionless velocity profiles ($u^+(y^+)$) in Fig. 4 reveal, flow suction reduces the width of the logarithmic layer and it affects the turbulent motions over the entire span of the boundary layer. Similar observations regarding the reduction of u_{rms} were also reported in Refs. [45–49, 58], therefore these findings are consistent with previous studies.

The inner peak recovers to the baseline levels of rms over a short downstream distance. Overall, a growth of σ is associated with a longer distance for the inner peak to recover to the baseline values of rms. The inner peak could present a mild overshooting as compared with the baseline case ($\sigma = 0$) when flow suction is applied ($\sigma > 0$). At $\alpha = 30°$, higher levels of u_{rms} are found for $\sigma > 0$, at BL1, BL2 and BL3 at $y^+ < 30$, i.e. in the buffer layer. The observed increase of the inner peak can be explained as a growth of the mean shear ($\mathrm{d}\bar{u}/\mathrm{d}y$), which is associated with decrease in the thickness of the boundary layer. At $\alpha = 70°$, the rms levels for $\sigma > 0$ remain below the baseline case ($\sigma = 0$) at all streamwise locations under analysis (BL1-BL3). At BL3, the magnitude of the rms at the inner peak is observed to increase and to move closer to the wall when suction is applied, which can be a consequence of the close proximity to the TE.

With the aim of showing the energy contributions of the different frequencies, the power spectral density (PSD) of the velocity fluctuations (ϕ_{uu}) is computed. To the purpose of the present investigation, it is particularly insightful to present the changes that flow suction produces on the velocity PSD, at different
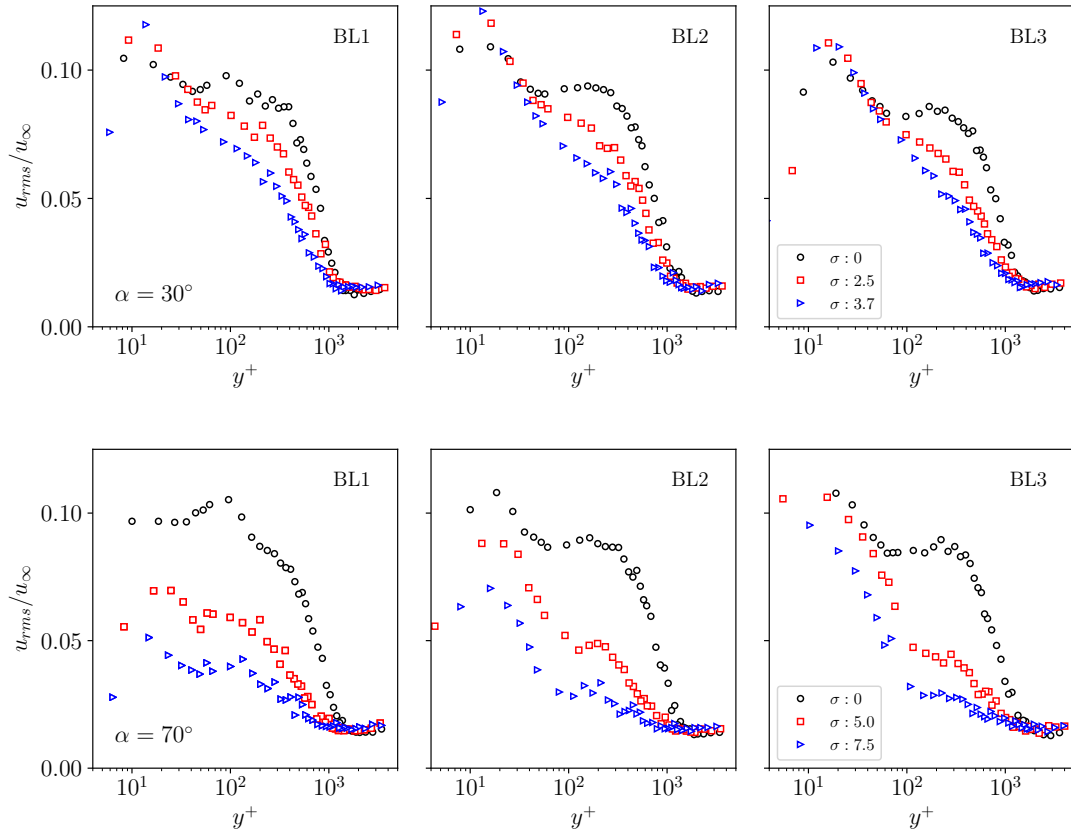
Figure 5: Profiles of the root mean square velocity as a function of dimensionless wall distance at flow control angles of $\alpha = 30°$ and $70°$ at locations BL1, BL2 and BL3.

downstream locations of the flow control treatment. The velocity PSD is calculated in the following way:

$$\phi_{uu} = 10 \log_{10} \left(\frac{|\hat{u}(f) \, (\hat{u}(f))^*|}{u_\infty^2} \right), \tag{6}$$

where $\hat{u}(f)$ is the fast Fourier transform of the velocity signal, the asterisk, *, denotes the complex conjugate, $|\ |$ is the absolute value operator, and u_∞ is the free-stream velocity. Figures 6 and 7 show the difference between the PSD of the velocity fluctuations in presence of the active flow control and the PSD of the velocity fluctuations for the baseline case:

$$\Delta\phi_{uu} = \phi_{uu,\sigma\neq0} - \phi_{uu,\sigma=0}. \tag{7}$$

From the velocity profiles presented in Figs. 4 and 5, the boundary layer was observed to change significantly as a consequence of flow suction, which would make it incorrect to subtract the two power spectral densities ($\phi_{uu,\sigma\neq0}$ and $\phi_{uu,\sigma=0}$) at the same physical wall-normal locations (y), because these physical locations correspond to different dimensionless wall-distances (y^+). To enable the subtraction between the values of power spectral densities at the same y^+, linear interpolations were applied from the existing values of power spectral densities to a new set of y^+. This new set of y^+ is bounded below by the largest y^+ of $\phi_{uu,\sigma\neq0}$ and $\phi_{uu,\sigma=0}$; and bounded above by the smallest y^+ of $\phi_{uu,\sigma\neq0}$ and $\phi_{uu,\sigma=0}$, therefore this new set of y^+ is not identical for the different cases under investigation. Analyzing these PSD differences at varying wall-normal locations enables us to determine the range of frequencies and wall-normal locations where the turbulent kinetic energy diminishes as a result of flow suction. This is at the basis of interpreting how the changes of the turbulence properties of the flow could lead to an attenuation of the surface pressure fluctuations, and therefore the estimated far-field noise.

In Fig. 6, the difference in the power spectral density ($\Delta\phi_{uu}$) is presented for flow suction at a flow control angle of $\alpha = 30°$, and for values of the flow control severity $\sigma = 2.5$ and $\sigma = 3.7$, at BL1, BL2 and BL3. As can be observed, flow suction reduces the energy content over a broad range of frequencies and wall-normal locations. At BL1 and for $\sigma = 2.5$, a significant reduction in ϕ_{uu} is observed in the logarithmic region ($30 < y^+ < 200$) and in the wake region ($200 < y^+ < 1000$), and this reduction is more significant at high frequencies ($f > 1$ kHz). From the $u^+(y^+)$ and $u_{rms}(y^+)$ velocity profiles, see Figs. 4 and 5, the observed reduction in the PSD can be attributed to a reduced extent of the logarithmic region when flow suction is applied. This is consistent with lower values of u_{rms} at the outer peak. Figure 6 reveals an increase in the energy content (ϕ_{uu}) at high frequencies ($f > 1$ kHz), at wall-normal locations corresponding to the
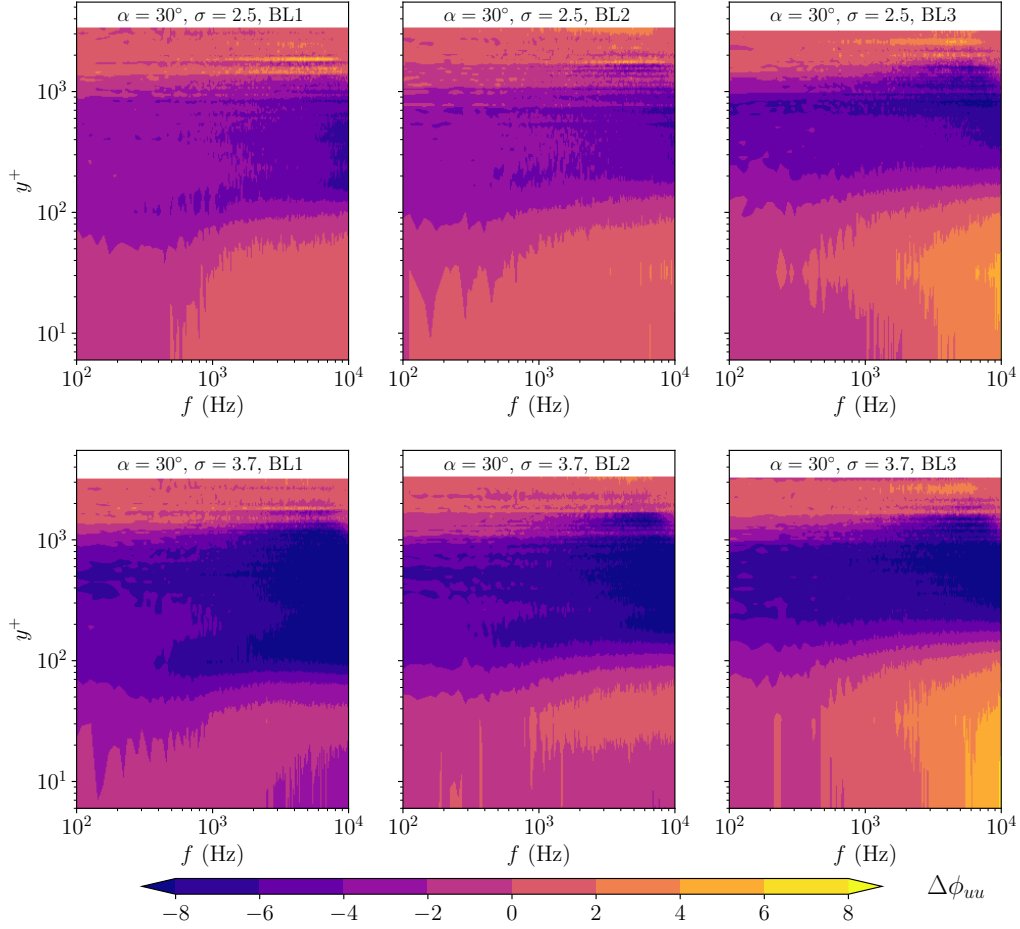
Figure 6: Changes in the velocity power spectral density at flow control angle $\alpha = 30°$ for $\sigma = 2.5$ and $\sigma = 3.7$ at locations BL1, BL2 and BL3.

inner peak ($y^+ \approx 30$). The spectral content is observed to grow at wall-normal locations below $y^+ \approx 30 - 40$ at all streamwise locations, i.e. at BL1, BL2 and BL3. These areas of increased PSD are consistent with the increase in u_{rms} at the inner peak ($y^+ \approx 30$) for $\sigma = 2.5$, see Figs. 5 and 6. At BL3, a significant increase in ϕ_{uu} is observed at $\sigma = 2.5$ at frequencies larger than $f \approx 1.4$ kHz and wall-normal locations below $y^+ = 100$. This observation is consistent with the increase of u_{rms} at the location of the inner peak, at BL3, see Fig. 5. The observed growth of the energy content could be an effect of the close presence of the TE, where the flow experiences a sudden change in the boundary conditions. At a larger value of suction severity ($\sigma = 3.7$), a broadband reduction of the spectral content can be observed at BL1. At BL2, however, a modest increase of $\Delta\phi_{uu}$ can be seen in Fig. 6 below $y^+ = 30$, which occurs at high frequencies ($f > 1$ kHz). In the close vicinity of the TE, at BL3, the velocity PSD exhibits the same behavior for $\sigma = 3.7$ as for $\sigma = 2.5$, i.e.

17

below $y^+ = 30$ an increase in ϕ_{uu} is observed at high frequencies ($f > 2$ kHz).

Figure 7 presents the difference of velocity PSD at flow control angle $\alpha = 70°$, and at $\sigma = 5.0$ and at $\sigma = 7.5$. At BL1, the velocity PSD is observed to decrease over all frequencies for wall-normal locations below $y^+ = 1000$, independent of σ. This is consistent with the reduced flow energy content at both inner and outer u_{rms} peak locations, see Fig. 5. At BL2, a lower amount of energy reduction takes place in the close vicinity of the wall ($y^+ \approx 30 - 40$), at low frequencies ($f < 1$ kHz). This indicates that the energy content of the inner peak increases as the flow travels downstream, and this energy increase is associated with the large-scale turbulent motions characterized by low frequencies ($f < 1$ kHz). For $\sigma = 5.0$ at the close vicinity of the TE (at BL3), the velocity PSD is observed to increase with respect to BL2 below $y^+ \approx 70$, and at high frequencies ($f > 2$ kHz). This increase in ϕ_{uu} is consistent with the u_{rms} results, where an increasing peak in the rms content is observed below $y^+ \approx 70$, see Fig. 5. The growth in the magnitude of the inner peak is broadband in nature, with a more pronounced increase at high frequencies ($f > 2$ kHz), which is the footprint of small scale structures. For $\alpha = 70°$, the larger suction severity ($\sigma = 7.5$) results in an almost complete elimination of flow energy content, especially at BL1. Downstream of BL1, a redevelopment of the inner peak can also be observed.

3.3. Effects of Flow Suction on the Surface Pressure Fluctuations

In the following paragraphs, the surface pressure spectra (ϕ_{pp}) are firstly presented, followed by the estimates of the spanwise extent of the turbulent length scales (Λ_z) and the velocity-pressure coherence (γ^2_{pu}). Given that the product between ϕ_{pp} and Λ_z drives the generation of TE noise [3], understanding how these quantities change as a result of flow suction is of main interest. In addition, the velocity-pressure coherence quantifies the impact of the different turbulent motions on the surface pressure fluctuations. These analyses clarify which changes of the turbulence properties can be considered responsible for the observed variations of the surface pressure fluctuations from flow suction.

Figure 8 presents the power spectral density of the surface pressure fluctuations (ϕ_{pp}, dB/Hz re. 20 μPa) for flow control angles $\alpha = 30°$ and $70°$, respectively. In addition, in measurements where flow control is applied, the spectra of Fig. 8 show the footprints of the facility's background noise. Specifically, the strong tonal peak observed at 3 kHz originates from the fan of the wind tunnel.

Overall, it can be observed that the spectral content of the surface pressure fluctuations is attenuated over a wide range of frequencies. At BL1, at an angle of $\alpha = 30°$ and at a flow severity of $\sigma = 2.5$, flow suction reduces the spectral content of the surface pressure fluctuations in the range of frequencies between 100 Hz and 4 kHz, above which only a modest increase (≈ 1 dB/Hz) of ϕ_{pp} is observed. At increasing
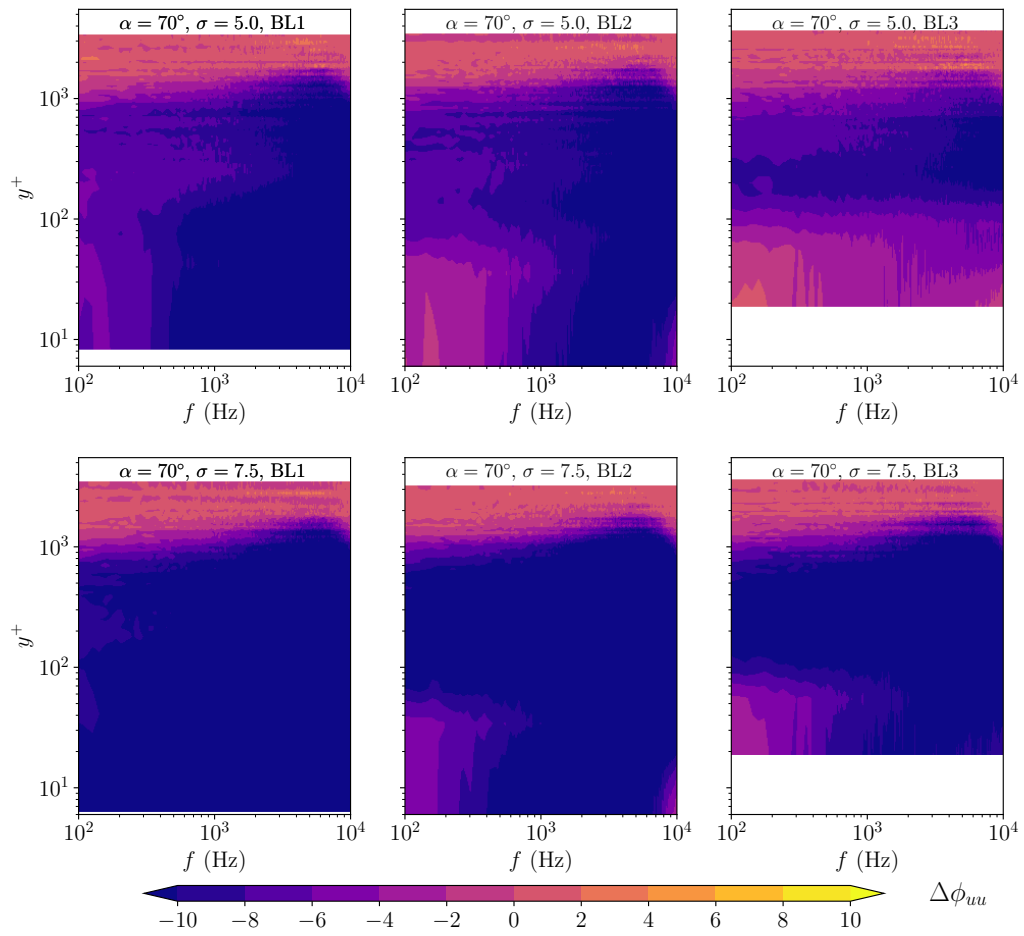
18

Figure 7: Changes of the velocity power spectral density at flow control angles $\alpha = 70°$ for $\sigma = 5.0$ and $\sigma = 7.5$, at locations BL1, BL2 and BL3.

19

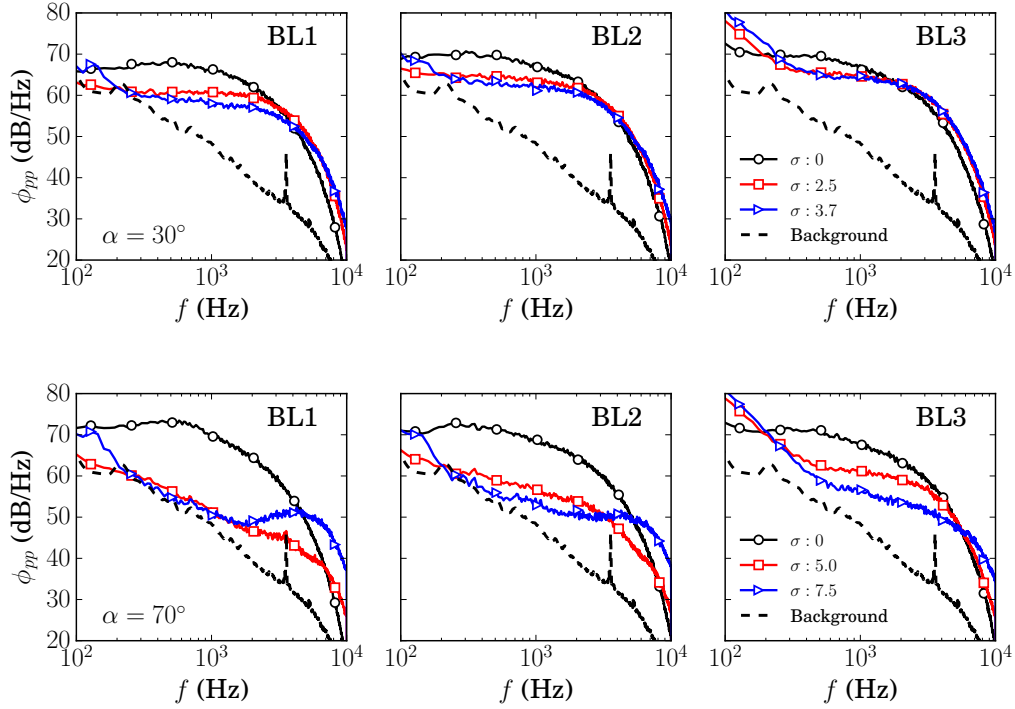Figure 8: Power spectral density, ϕ_{pp} (dB/Hz, re. 20 μPa), of the surface pressure fluctuations at flow control angles $\alpha = 30°$ and $\alpha = 70°$ at locations BL1, BL2 and BL3.

downstream locations (BL2 and BL3), the spectral content (ϕ_{pp}) exhibits a broadband increase compared to BL1, which can be explained as a result of flow recovery. The recovery of the flow downstream of flow suction reduces the frequency range where the positive effects of the flow control can be obtained at the TE. At BL3 and for $\sigma = 2.5$, the range of frequencies where a reduction of ϕ_{pp} is observed is found between 200 Hz and 1.4 kHz. The PSD of the surface pressure can be related to the behavior of the velocity PSD formerly seen in Fig. 6. For $\sigma = 2.5$, a broadband reduction is achieved of both the velocity and the surface pressure PSD downstream of the flow control treatment (BL1-BL3), in the frequency range of 100-2000 Hz. Both u_{rms} and ϕ_{uu} suggest that the reduction in the low and mid-frequencies is associated with the reduction of both the size and energy content of the logarithmic layer. The observed increase of the spectral contents at high frequencies, namely above $f \approx 4$ kHz at BL1 and BL2, and above 1.4 kHz at BL3, is associated with the increased energy content at the inner peak ($y^+ \approx 30$). Therefore, it can be concluded that the footprint of the small-scale near-wall turbulent motions are responsible for the increased energy content of the surface pressure fluctuations at high-frequencies, when low suction rates ($\sigma = 2.5$ and 3.7) are applied.

A larger energy content is found at low frequencies, i.e. below 200 Hz, at the close vicinity of the

20

TE (BL3), regardless of the applied flow suction severity. The surface pressure PSD exhibits a sudden increase below $f = 200$ Hz only at BL3, which confirms that the effect is not induced by acoustic pressure fluctuations. Nonetheless, a similar amount of growth within the spectral content at low frequencies is not observed when looking at the velocity spectrum (ϕ_{uu}). This strongly suggests that the observed low-frequency increase of ϕ_{pp} is not caused by flow turbulence. Therefore, further investigations, such as large eddy simulations or direct numerical simulations, are required to shed light on the underlying physics of the observed low-frequency increase in the surface pressure spectra.

At $\alpha = 70°$, the reduction of the spectral content ϕ_{pp} takes place over a wider range of frequencies. At BL1, the measured spectral content collapses on the level of the background noise above $\sigma \approx 6.0$. For $\alpha = 70°$ at $\sigma = 7.5$, a broadband hump is observed at BL1 between $f = 2$ kHz and $f = 10$ kHz, which persists at BL2, even though at lower amplitudes. This observation is further investigated in the analysis of the velocity-pressure coherence (γ_{pu}^2).
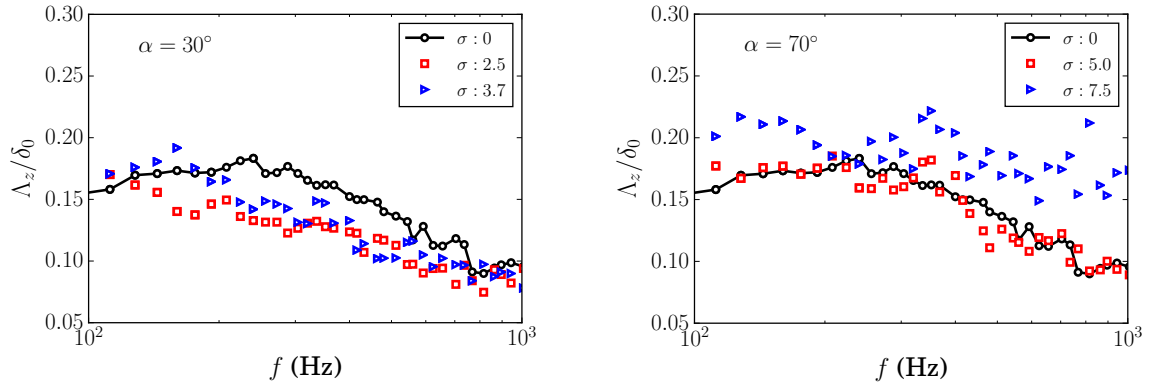

Figure 9: Estimation of spanwise extent of turbulent structures $x/\delta_0 = 0.4$ upstream of the TE for $\alpha = 30°$ and $\alpha = 70°$.

In the following, an estimate of Λ_z is presented. In order to understand how the inclined flow suction affects the far-field noise, its effect on the spanwise extent of the turbulent structures is investigated with the help of Fig. 9. In the case of $\alpha = 30°$, a broadband reduction of Λ_z is obtained above $f \approx 130$ Hz, for both investigated cases of flow suction severity. This is in agreement with u_{rms} results, as this implies the presence of smaller turbulent structures with respect to the baseline case. At increased angles and values of flow suction severity, the spanwise extent of turbulent structures show a broadband increase. At $\sigma = 5.0$, which is still below the saturation point ($\sigma \approx 6$), Λ_z is similar to that of the baseline case. Above $\sigma \approx 6$, the estimated size of turbulent structures increase at all frequencies. Amiet's model [3] considers a turbulent boundary layer, and it is valid under the assumption of Taylor's hypothesis of frozen turbulence. Therefore,

estimating Λ_z using Eq. (5) above the saturation point of $\sigma \approx 6$, where the boundary layer significantly departs from a canonical turbulent boundary layer, could lead to some unexpected deviations from the underlying physics. In this context, the observed broadband increase in Λ_z above $\sigma \approx 6$ might fails to provide physical information about the spanwise extent of the turbulent structures. In addition, at these severe suction rates ($\sigma > 6$), the signal to noise ratio between the hydrodynamic pressure fluctuations of the boundary layer and the background noise might falls below the range of 8-10 dB, which could potentially violate the reliability of the Λ_z results. Considering the estimated far-field noise, see Fig. 2, and the surface pressure spectra, it can be concluded that the attenuation of the term ϕ_{pp} as a result of flow suction is stronger than the increase of Λ_z, which results in a reduction of the estimated noise.

As observed up until now, boundary layer suction alters the spectral content of both velocity and pressure fluctuations. To examine the spectral content of the velocity-pressure interaction, the coherence (normalized cross-spectra, γ_{pu}^2) was calculated between the velocity and surface pressure signals at different streamwise (BL1,BL2 and BL3) and wall-normal locations (y^+). The velocity-pressure coherence can be calculated as:

$$\gamma_{pu}^2 = \frac{|\hat{p}(f)\,\hat{u}(f)|^2}{\phi_{pp}\phi_{uu}}, \tag{8}$$

where $\hat{p}(f)$ and $\hat{u}(f)$ are the Fast Fourier Transform (FFT) of the pressure $p(t)$ and velocity $u(t)$ time signals, respectively, and $|\,|$ is the absolute value operator. From a physical point of view, the velocity-pressure coherence (γ_{pu}^2) represents the frequency dependent relationship between the turbulent motions and the surface pressure fluctuations.

To determine the contribution of the different regions of the boundary layer to the surface pressure spectrum (ϕ_{pp}) in the absence of flow control, the velocity-pressure coherence for the baseline boundary layer ($\sigma = 0$) is presented in Fig. 10. As can be observed, the turbulence motions located at decreasing distances from the wall play an increasing effect on the surface pressure fluctuations. A significant contribution to ϕ_{pp} originates from the velocity fluctuations below the logarithmic layer ($y^+ < 20$), over the entire range of the investigated frequencies. The logarithmic layer ($20 < y^+ < 300$) also plays a significant role on γ_{pu}^2 at low frequencies ($f < 1$ kHz). Finally, the wake layer ($300 < y^+ < 2000$), where the largest turbulent motions are located, is associated with the low frequency portion of the pressure spectrum.

Figures 11 and 12 present the velocity-pressure coherence (γ_{pu}^2) for $\alpha = 30°$ and $70°$, respectively, over the entire span of the boundary layer thickness, at BL1, BL2 and BL3. When flow suction is applied, the velocity-pressure coherence (γ_{pu}^2) undergoes changes as compared to the coherence associated with the
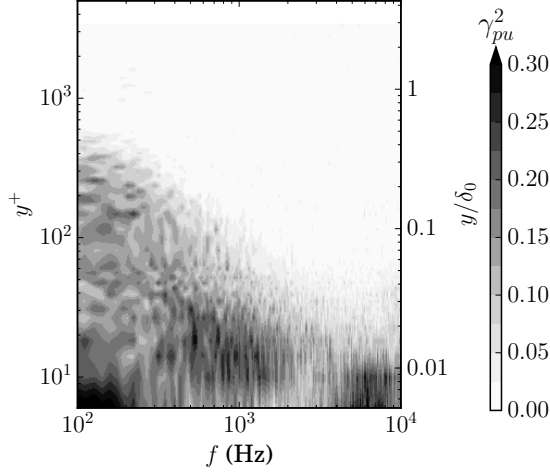
Figure 10: Velocity-pressure coherence for the baseline case ($\sigma = 0$) at BL3.

turbulent boundary layer in the absence of flow control. Firstly, the results obtained from the $\alpha = 30°$ flow control angle are discussed, see Fig. 11.

At BL1 for $\sigma = 2.5$, the velocity-pressure coherence map reveals that the contribution of the velocity fluctuations within the buffer layer ($y^+ < 20$) becomes stronger when flow suction is applied. At BL1, four different islands of high coherence can be identified, which are also marked with boxes of red dashed lines in Fig. 11. Two areas of high coherence are visible at low frequencies, i.e. $f < 500$ Hz, one between $y^+ = 30$ and $y^+ = 300$ and one below $y^+ = 30$. In the range between 500 Hz and 3 kHz, a region of high γ^2_{pu} is found at $10 < y^+ < 40$. Finally, a region of high coherence is visible at high frequencies ($f > 3$ kHz) at $y^+ < 20$. The coherence observed at low frequencies ($f < 500$ Hz) between $y^+ = 30$ and $y^+ = 300$ represents the effects of the turbulent motions within the logarithmic region on the surface pressure fluctuations. When compared to the baseline case, flow suction reduces the communication between the velocity fluctuations and the pressure fluctuations within the logarithmic region. On the other hand, the very high levels of γ^2_{pu} at $y^+ < 40$ could be the result of the increased velocity gradient ($d\bar{u}/dy$), which is observed to enhance the energy content (u_{rms}) within this region of the boundary layer, see Fig. 5. The observed increase at high frequencies ($f > 3$ kHz, $y^+ < 20$) coincides with the area where an increase in $\Delta\phi_{uu}$ was also found in Fig. 6. Therefore, the contribution of the velocity fluctuations to the surface pressure fluctuations above $f = 3$ kHz and below $y^+ = 20$ also confirms that the turbulent motions below the logarithmic layer ($y^+ < 30$) are responsible for the increase of ϕ_{pp} (see Fig. 8) at the same range of frequencies ($f > 3$ kHz).

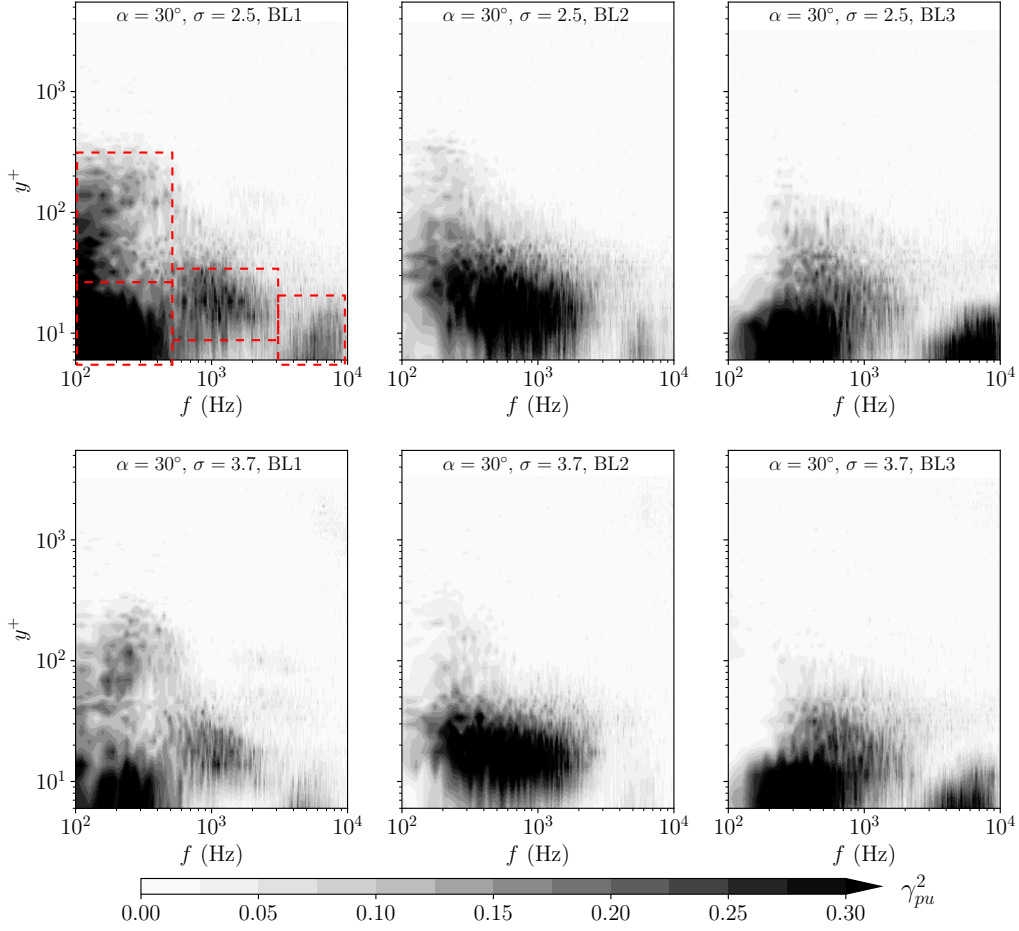At BL2 for $\sigma = 2.5$ and $\alpha = 30°$, the structure of γ^2_{pu} changes significantly compared to BL1. At low

Figure 11: Velocity-pressure coherence at flow control angle $\alpha = 30°$ and flow suction severity for $\sigma = 2.5$ and $\sigma = 3.7$ at locations BL1, BL2 and BL3. The red boxes indicate areas of high coherence.

frequencies ($f < 500$ Hz), the magnitude of γ_{pu}^2 decreases in the logarithmic layer ($30 < y^+ < 300$) as compared with BL1, which shows that the footprint of the velocity fluctuations within the logarithmic layer on the surface pressure decreases when moving from BL1 to BL2. This observation also confirms that the turbulent kinetic energy reduces in the logarithmic region as a consequence of flow suction. At BL2, the low-frequency area ($f < 500$ Hz) of high coherence shows significantly lower levels of γ_{pu}^2 below $y^+ = 20$, but a larger spectral content can be observed in the region of $10 < y^+ < 50$ and 200 Hz $< f < 2$ kHz. The wall-normal locations of strong communication match well with the locations of high u_{rms} observed in Fig. 5. This also reveals that the turbulent motions are enhanced by flow suction at the location of the inner peak. The observed changes in the velocity-pressure coherence between BL1 and BL2 suggest that the major

24

contribution to the surface pressure fluctuations originates from the inner peak at BL2, as a consequence of flow suction. This is different from the baseline case, where each region of the boundary layer (buffer, logarithmic and wake) was found to provide comparable contributions to the surface pressure fluctuations.

Finally, at BL3, the coherence map shows slightly different features as compared to the locations BL1 and BL2. The u_{rms} profiles in Fig. 5 show that at BL3 the inner peak moves closer to the wall with respect to the baseline case. The velocity-pressure coherence results at BL3 are consistent with this observation, where the mid-frequency region of high coherence ($6 < y^+ < 20$ and 100 Hz $< f <$1 kHz) is found at lower levels of dimensionless wall distance with respect to locations BL1 or BL2. Additionally, an area of high coherence is observed at high frequencies above $f > 2$ kHz and below $y^+ = 20$, which is in agreement with the increase in ϕ_{pp} and ϕ_{uu} at high-frequencies, see Figs. 6 and 8. These two mid- and high-frequency regions of high coherence are isolated from each other in terms of their associated frequency, as very low coherence ($\gamma^2_{pu} < 0.05$) is found between these two islands of high γ^2_{pu}. This observation suggests that the flow structures leading to these two islands of high coherence are independent of each other, even though they are found at nearly the same distance from the wall. Also, at both BL2 and BL3, low levels of coherence are observed in the logarithmic region ($20 < y^+ < 300$), which also confirms the reduction of turbulent kinetic energy in this region as a result of flow suction. At $\sigma = 3.7$, the pattern of the velocity-pressure coherence remains very similar to the one obtained at $\sigma = 2.5$, see Fig. 11. The coherence decreases in the regions of high intensity when compared with the corresponding spectra for $\sigma = 2.5$. This observation is in agreement with the PSD of both velocity and surface pressure, where a larger reduction is found at increasing rates of flow control severity, σ.

For $\alpha = 70°$ and $\sigma = 5.0$ at BL1 (Fig. 12), the two areas of high coherence observed for $\alpha = 30°$ merge into one at low frequencies ($f < 500$ Hz), below $y^+ < 300$. At mid-frequencies, γ^2_{pu} is characterized by lower values than at $\alpha = 30°$. This is in agreement with the lower flow energy content at mid-frequencies previously observed for ϕ_{uu}. On the other hand, the high-frequency area of high coherence ($f > 2$ kHz and $y^+ < 20$) is not observed at BL1 in Fig. 12, which is consistent with the reduction observed in ϕ_{pp} at high frequencies, see Fig. 8. At BL2, the same pattern of γ^2_{pu} is observed for the two angles $\alpha = 70°$ and $\alpha = 30°$, see Fig. 11. Independent of the flow control angle, an increase in the flow control severity (σ) produces the same effects on the velocity-pressure coherence, which can be observed by comparing the two cases of suction severity ($\sigma = 5.0$ and $\sigma = 7.5$) shown in Fig. 12. In particular, the spectral content at BL3 diminishes at increasing values of flow control severity, which is an indication of a saturation in coherence reduction caused by flow suction. This is due to a significant amount of reduction of both velocity and
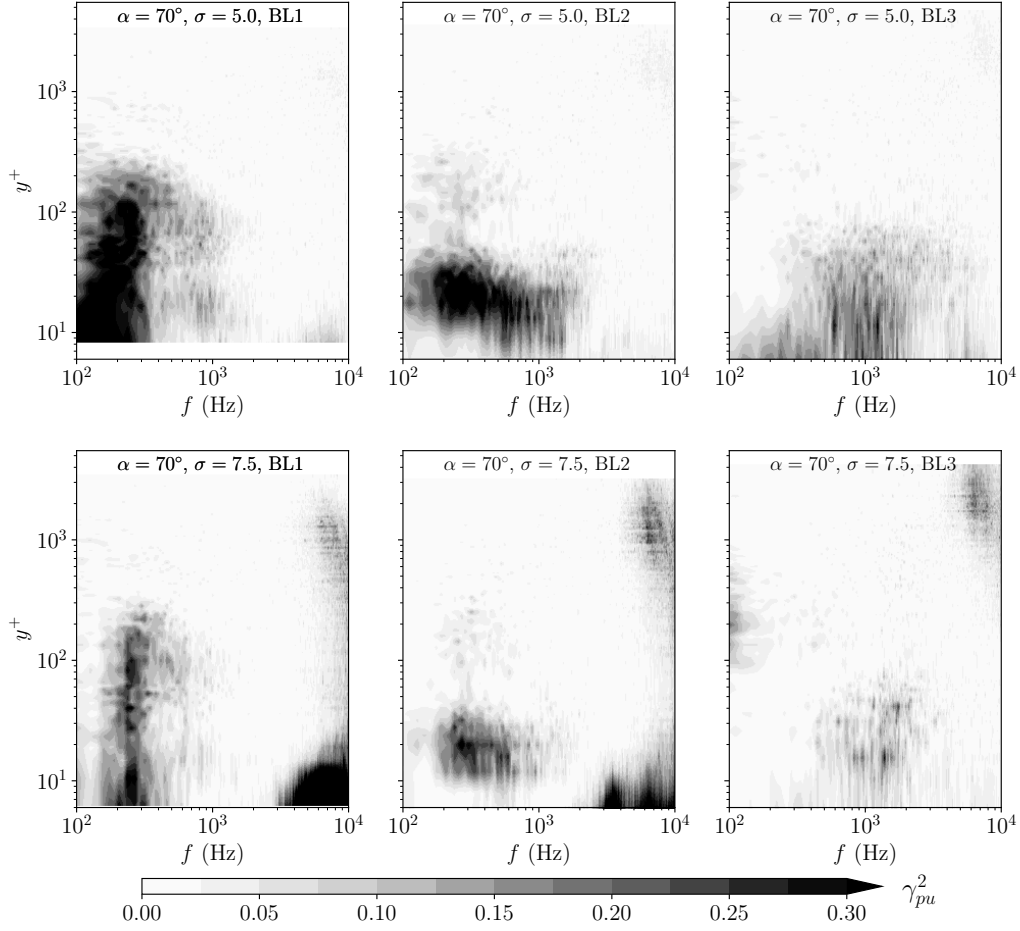
Figure 12: Velocity-pressure coherence at flow control angle $\alpha = 70°$ and flow suction severity $\sigma = 5.0$ and $\sigma = 7.5$ at locations BL1, BL2 and BL3.

pressure fluctuations. This observation is in agreement with the values obtained earlier for the quantities u_{rms}, ϕ_{uu}, and ϕ_{pp}. Nonetheless, some exceptions to this trend are observed. For example, at BL1, at $\alpha = 70°$ and $\sigma = 7.5$, see Fig. 12, the high-frequency ($f > 2$ kHz) area of high coherence below $y^+ = 20$ exhibits higher levels of coherence than at lower σ, for a constant flow control angle (α). This area of high coherence matches the increase of the pressure spectral content (ϕ_{pp}) at high frequencies ($f = 2 - 10$ kHz), see Fig. 8. This effect still persists downstream, at BL2. The observation suggests that the broadband humps in ϕ_{pp} above $f = 2$ kHz are associated with near-wall high-frequency turbulent motions.

4. Conclusions

The current work investigated the effects of flow suction on the generation of trailing edge noise. Experiments were conducted at a free-stream velocity of 15 m/s at the open-jet closed-loop wind tunnel of the University of Bristol. To this purpose, uniform inclined flow suction was applied on a flat plate rig upstream of a sharp trailing edge with the aim of controlling the hydrodynamic pressure field associated with the turbulent boundary layer. The simultaneous measurement of velocity with hot-wire anemometry and surface pressure fluctuations with flush-mounted microphones was performed at a number of locations downstream of the flow suction area. Results were collected at a range of flow suction severity rates ($\sigma = 0 - 9.1$), which relates the momentum deficit of the uncontrolled boundary layer to the momentum of the flow suction. The flow suction was applied at different angles with respect to the free-stream velocity, namely at $\alpha = 30°$, $50°$, $70°$ and $90°$. Inclination to the flow suction velocity was achieved using a honeycomb material with inclined pores. The honeycomb structure was covered with a fine steel wire-mesh, which was chosen such that it did not introduce any energy increase to the unsteady surface pressure fluctuations downstream of the flow control area.

The estimation of far-field trailing edge noise using Amiet's model [3] showed that inclined uniform flow suction reduces the overall sound pressure level in all cases under investigation. In more details, the trailing edge noise was found to reduce at frequencies between 200 Hz and 2-3 kHz, with penalties observed outside of this frequency range. As the flow suction severity and the inclination angle increased, the reduction at mid-frequencies improved while the level of penalties did not change significantly. Overall, flow suction at an angle of $\alpha = 70°$ and $\sigma \approx 6$ was found to exhibit the best performance in reducing the noise levels. Increasing the suction severity above this point failed to further reduce the estimated far-field noise.

The streamwise velocity profiles showed that flow suction reduces the thickness of the turbulent boundary layer, and therefore, the wall-normal extent of the different regions constituting the boundary layer flow, namely the buffer layer, the logarithmic region, and the wake region. In agreement with this, flow suction reduces the energy content of the turbulent boundary layer over its entire span with the most significant amount of energy reduction obtained within the logarithmic region. On the other hand, the resulting thinner boundary layer is characterized by an increased level of mean shear, particularly below the logarithmic layer. These effects increase with the flow suction severity until a saturation in the profiles is observed at $\sigma \approx 6$, but beyond this point, no additional benefits can be obtained from further increasing σ.

The velocity power spectral density (PSD) downstream of the flow control treatment indicated a significant amount of reduction in the boundary layer energy content over the entire range of investigated

frequencies. In particular, the velocity PSD was observed to decrease most significantly at mid and high frequencies, which was associated with the reduction of the flow energy content within the logarithmic region. Increase in the velocity PSD was observed at the near-wall regions of the boundary layer at high frequencies, which was due to the increased energy content within the buffer layer.

The changes in the turbulent statistics have profound effects on the hydrodynamic pressure field. Flow suction efficiently reduces the energy content of the surface pressure fluctuations over a wide range of frequencies, which is mainly due to the reduction of the size of the logarithmic layer, and its energy content. The increased shear in the near-wall region causes penalties at high-frequencies in the surface pressure power spectra, and therefore, in the predicted far-field trailing edge noise. The velocity-pressure coherence also confirmed that the contribution of the turbulent motions to the surface pressure fluctuations rearranges within the boundary layer due to flow suction. Due to the drop in the size and flow energy content of the logarithmic layer, the footprint of the turbulent motions on the surface pressure fluctuations originated from the logarithmic layer also reduces. On the other hand, the contribution to the surface pressure fluctuations from the turbulent motions located below the logarithmic layer becomes more dominant. These trends were found to increase until $\sigma \approx 6$, where a saturation in the changes of turbulence quantities were found. Above this point, no further aeroacoustic benefits can be obtained with further increasing the flow suction severity.

Declaration of interest

The authors report no conflict of interest.

References

[1] T. F. Brooks, D. S. Pope, M. A. Marcolini, Airfoil self-noise and prediction, NASA Rep. 1218 (1989).

[2] T. F. Brooks, T. H. Hodgson, Trailing edge noise prediction from measured surface pressures, J. Sound Vib. 78 (1) (1981) 69–117.

[3] R. K. Amiet, Noise due to turbulent flow past a trailing edge, J. Sound Vib. 47 (3) (1976) 387–393.

[4] B. Arnold, T. Lutz, E. Krämer, C. Rautmann, Wind-turbine trailing-edge noise reduction by means of boundary-layer suction, AIAA J. 56 (5) (2018) 1843–1854.

[5] A. Wolf, T. Lutz, W. Würz, E. Krämer, O. Stalnov, A. Seifert, Trailing edge noise reduction of wind turbine blades by active flow control, Wind Energy 18 (5) (2014) 909–923.

[6] R. K. Amiet, Acoustic radiation from an airfoil in a turbulent stream, J. Sound Vib. 41 (4) (1975) 407–420.

[7] M. Howe, On the Added Mass of a Perforated Shell, with Application to the Generation of Aerodynamic Sound by a Perforated Trailing Edge, Proc. R. Soc. Lond. Ser. A, Math. Phys. Sci. 365 (1721) (1979) 209–233.

[8] R. R. Parchen and Technisch Physisce Dienst, Progress report DRAW: A prediction scheme for trailing edge noise based on detailed boundary layer characteristics, TNO Rep. (HAG-RPT-980023) (1998).

[9] M. S. Howe, A review of the theory of trailing edge noise, J. Sound Vib. 61 (3) (1978) 437–465.

[10] B. Lyu, M. Azarpeyvand, S. Sinayoko, Prediction of noise from serrated trailing edges, J. Fluid Mech. 793 (2016) 556–588.

[11] M. Wang, Computation of trailing-edge noise at low Mach number using LES and acoustic analogy, Centre for Turbulence Research, Annual Research Briefs (1998) 91–105.

[12] M. Wang, P. Moin, Computation of trailing-edge flow and noise using large-eddy simulation, AIAA J. 38 (12) (2000) 2201–2209.

[13] R. Ewert, W. Schroeder, On the simulation of trailing edge noise with a hybrid LES/APE method, J. Sound Vib. 270 (3) (2004) 509–524.

[14] W. R. Wolf, S. K. Lele, Trailing-edge noise predictions using compressible large-eddy simulation and acoustic analogy, AIAA J. 50 (11) (2012) 2423–2434.

[15] M. Gruber, Airfoil noise reduction by edge treatments, Ph.D. thesis, University of Southampton, United Kingdom (2012).

[16] X. Liu, H. J. Kamliya, M. Azarpeyvand, R. Theunissen, Wake Development of Airfoils with Serrated Trailing Edges, 22nd AIAA/CEAS Aeroacoustics Conf., Lyon, France (AIAA-2016-2817).

[17] T. Chong, A. Vathylakis, P. Joseph, M. Gruber, Self-noise produced by an airfoil with nonflat plate trailing-edge serrations, AIAA J. 51 (11) (2013) 2665–2677.

[18] T. Chong, P. Joseph, An experimental study of airfoil instability tonal noise with trailing edge serrations, J. Sound Vib. 332 (24) (2013) 6335–6358.

[19] T. Chong, P. Joseph, M. Gruber, Airfoil self noise reduction by non-flat plate type trailing edge serrations, Appl. Acoust. 74 (4) (2013) 607–613.

[20] M. Gruber, P. Joseph, M. Azarpeyvand, An experimental investigation of novel trailing edge geometries on airfoil trailing edge noise reduction, 19th AIAA/CEAS Aeroacoustics Conf., Berlin, Germany (AIAA-2013-2011).

[21] M. Azarpeyvand, M. Gruber, P. Joseph, An analytical investigation of trailing edge noise reduction using novel serrations, 19th AIAA/CEAS Aeroacoustics Conf., Berlin, Germany (AIAA-2013-2009).

[22] A. Finez, E. Jondeau, M. Roger, M. Jacob, Broadband noise reduction with trailing edge brushes, 16th AIAA/CEAS Aeroacoustics Conf., Stockholm, Sweden (AIAA-2010-3980).

[23] M. Herr, W. Dobrzynski, Experimental investigations in low-noise trailing-edge design, AIAA J. 43 (6) (2005) 1167–1175.

[24] T. Geyer, E. Sarradj, C. Fritzsche, Porous airfoils: noise reduction and boundary layer effects, 15th AIAA/CEAS Aeroacoustics Conf., Miami, Florida (AIAA-2009-3392).

[25] T. Geyer, E. Sarradj, C. Fritzsche, Measurement of the noise generation at the trailing edge of porous airfoils, Exp. Fluids 48 (2) (2010) 291–308.

[26] S. A. Showkat Ali, M. Azarpeyvand, C. R. Ilário da Silva, Trailing-edge flow and noise control using porous treatments, J. Fluid Mech. 850 (2018) 83–119.

[27] S. Showkat Ali, X. Liu, M. Azarpeyvand, Bluff body flow and noise control using porous media, 22nd AIAA/CEAS Aeroacoustics Conf., Lyon, France (AIAA-2016-2754).

[28] S. A. Showkat Ali, M. Szőke, M. Azarpeyvand, Trailing edge bluntness flow and noise control using porous treatments, 22nd AIAA/CEAS Aeroacoustics Conf., Lyon, France (AIAA-2016-2832).

[29] S. A. Showkat Ali, M. Azarpeyvand, M. Szőke, C. R. Ilário da Silva, Boundary layer flow interaction with a permeable

wall, Phys. Fluids 30 (8) (2018) 085111.

[30] H. Liu, M. Azarpeyvand, J. Weia, Z. Qua, Tandem cylinder aerodynamic sound control using porous coating, J. Sound Vib. 334 (2014) 190–201.

[31] A. Afshari, M. Azarpeyvand, A. A. Dehghan, M. Szőke, Trailing edge noise reduction using novel surface treatments, 22nd AIAA/CEAS Aeroacoustics Conf., Lyon, France (AIAA-2016-2834).

[32] A. Afshari, M. Azarpeyvand, A. A. Dehghan, M. Szőke, Three-dimensional surface treatments for trailing edge noise reduction, 23rd International Congress on Sound & Vibration, Athens, Greece (2016).

[33] I. Clark, D. Baker, W. N. Alexander, W. Devenport, S. A. Glegg, J. Jaworski, N. Peake, Experimental and theoretical analysis of bio-inspired trailing edge noise control devices, 22nd AIAA/CEAS Aeroacoustics Conf., Lyon, France (AIAA-2016-3020).

[34] I. Clark, W. N. Alexander, W. Devenport, S. A. Glegg, J. Jaworski, C. Daily, N. Peake, Bio-inspired trailing edge noise control, 21nd AIAA/CEAS Aeroacoustics Conf., Dallas, Texas (AIAA-2015-2365).

[35] A. Afshari, M. Azarpeyvand, A. A. Dehghan, M. Szőke, R. Maryami, Trailing-edge flow manipulation using streamwise finlets, J. Fluid Mech. 870 (2019) 617–650.

[36] Q. Ai, M. Azarpeyvand, X. Lachenal, P. M. Weaver, Aerodynamic and aeroacoustic performance of airfoils with morphing structures, Wind Energy 19 (7) (2016) 1325–1339.

[37] P. M. Hartwich, E. D. Dickey, A. J. Sclafani, P. Camacho, A. B. Gonzales, E. L. Lawson, R. Y. Mairs, A. Shmilovich, AFC-enabled simplified high-lift system integration study, NASA Tech. Rep. NASA/CR-2014-218521 (2014).

[38] M. K., Effect of a coanda extension on the performance of a sweeping jet actuator, AIAA J. 54 (3) (2016) 1125–1128.

[39] T. Lutz, B. Arnold, A. Wolf, E. Krämer, Numerical studies on a rotor with distributed suction for noise reduction, J. Phys: Conf. Ser. 524 (1) (2014) 012122.

[40] D. Matera, Validation of the noise prediction code rnoise and reduction of trailing edge noise by active flow control, Ph.D. thesis, Universita Degli Studi Di Padova, Italy (2013).

[41] B. Arnold, C. Rautmann, T. Lutz, E. Kraemer, Design of a boundary-layer suction system for trailing-edge noise reduction of an industrial wind turbine, 35th Wind Energy Symposium, Grapevine, Texas (AIAA-2017-1380).

[42] M. Szőke, D. Fiscaletti, M. Azarpeyvand, Effect of inclined transverse jets on trailing-edge noise generation, Phys. Fluids 30 (8) (2018) 085110.

[43] S. Moreau, P. Laffay, A. Idier, N. Atalla, Several noise controls of the trailing-edge noise of a controlled-diffusion airfoil, 22nd AIAA/CEAS Aeroacoustics Conf., Lyon, France (AIAA-2016-2816).

[44] R. A. Antonia, L. Fulachier, L. V. Krishnamorthy, T. Benabid, F. Anselmet, Influence of wall suction on the organized motion in a turbulent boundary layer, Journal of Fluid Mechanics 190 (1988) 217–240.

[45] R. A. Antonia, Y. Zhu, M. Sokolov, Effect of concentrated wall suction on a turbulent boundary layer, Phys. Fluids 7 (10) (1995) 2465–2474.

[46] O. Oyewola, L. Djenidi, R. Antonia, Combined influence of the Reynolds number and localised wall suction on a turbulent boundary layer, Exp. Fluids 35 (2) (2003) 199–206.

[47] O. Oyewola, L. Djenidi, R. A. Antonia, Influence of localised wall suction on the anisotropy of the Reynolds stress tensor in a turbulent boundary layer, Exp. Fluids 37 (2) (2004) 187–193.

[48] O. Oyewola, L. Djenidi, R. Antonia, Influence of localised double suction on a turbulent boundary layer, J. Fluid Struct. 23 (5) (2007) 787–798.

[49] J. Park, H. Choi, Effects of uniform blowing or suction from a spanwise slot on a turbulent boundary layer flow, Phys. Fluids 11 (10) (1999) 3095–3105.

[50] Y. Kametani, K. Fukagata, R. Örlü, P. Schlatter, Effect of uniform blowing/suction in a turbulent boundary layer at moderate reynolds number, International Journal of Heat and Fluid Flow 55 (2015) 132–142.

[51] M. Szőke, M. Azarpeyvand, Active flow control methods for the reduction of trailing edge noise, 23rd AIAA/CEAS Aeroacoustics Conf., Denver, Colorado (AIAA-2017-3004).

[52] M. Szőke, Trailing edge noise control using active flow control methods, Ph.D. thesis, University of Bristol (2019).

[53] M. Roger, S. Moreau, Broadband self-noise from loaded fan blades, AIAA J. 42 (3) (2004) 536–544.

[54] D. Spalding, A single formula for the law of the wall, J. Appl. Mech. 28 (3) (1961) 455–458.

[55] P. Schlatter, R. Örlü, Assessment of direct numerical simulation data of turbulent boundary layers, J. Fluid Mech. 659 (2010) 116–126.

[56] S. B. Pope, Turbulent flows, IOP Publishing, Cambridge University Press, United Kingdom, 2001.

[57] A. J. Smits, B. J. McKeon, I. Marusic, High-Reynolds number wall turbulence, Annu. Rev. Fluid Mech. 43 (2011) 353–375.

[58] L. Djenidi, A. Agrawal, R. Antonia, Anisotropy measurements in the boundary layer over a flat plate with suction, Exp. Ther. Fluid Sci. 33 (7) (2009) 1106–1111.